Electronic Supplementary Material (ESI) for Journal of Materials Chemistry A.

SUPPORTING INFORMATION

Manganese-Cobalt Hexacyanoferrate Cathodes for Sodium-ion Batteries

Mauro Pasta[1,2†], Richard Y. Wang[1†], Riccardo Ruffo[3], Ruimin Qiao[4], Hyun-Wook Lee[1], Badri Shyam[5], Minghua Guo[4,6], Yayu Wang[6], L. Andrew Wray[7], Wanli Yang[4], Michael F. Toney[5] and Yi Cui[1,8*]

[1]Department of Materials Science and Engineering, Stanford University, Stanford, California 94305, USA.
[2]Department of Materials, University of Oxford, Oxford, OX1 3PH, UK.
[3]Dipartimento di Scienza dei Materiali, Università degli Studi di Milano-Bicocca, Via Cozzi 53, 20125 Milano, Italy.
[4]Advanced Light Source, Lawrence Berkeley National Laboratory, Berkeley, CA 94720, USA
[5]Stanford Synchrotron Radiation Lightsource, SLAC National Accelerator Laboratory, Menlo Park, California 94025, USA.
[6]State Key Lab of Low-Dimensional Quantum Physics, Department of Physics, Tsinghua University, Beijing 100084, P.R. China.
[7]Department of Physics, New York University, New York, New York 10003, USA
[8]Stanford Institute for Materials and Energy Sciences, SLAC National Accelerator Laboratory, 2575 Sand Hill Road, Menlo Park, California 94025, USA.

---

[*] Corresponding Author: yicui@stanford.edu
[†] These authors contributed equally

Methods

Cobalt-Manganese hexacyanoferrates synthesis. Preparation of nanoparticulate cobalt-manganese hexacyanoferrates was based on a previously reported synthesis procedures [7]. Briefly, equal volumes of 40 mM $Co(NO_3)_2$ (Alfa Aesar) and 20 mM $K_4Fe(CN)_6$ (Sigma Aldrich) were combined by simultaneous, dropwise addition into water under vigorous stirring in a 5M NaCl solution. The Co-MnHCFe was filtered, washed with water, and dried in vacuum at 100^0C overnight.

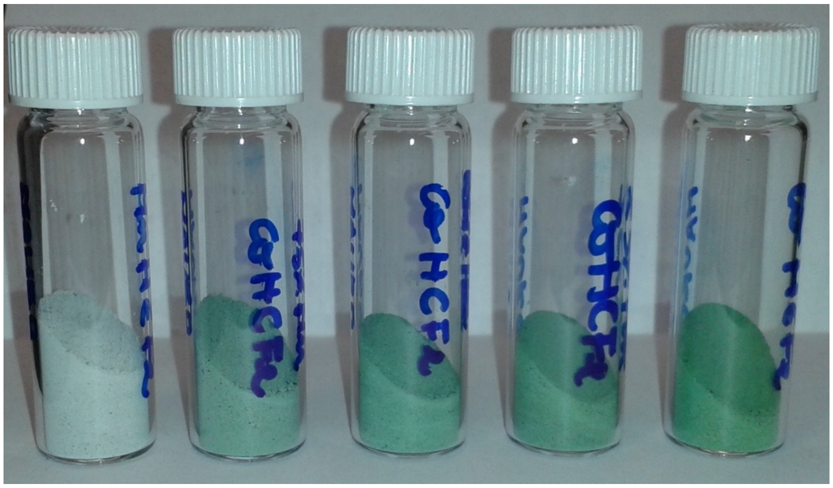

From left to right: MnHCFe. 25%Co-MnHCFe, 50% Co-MnHCFe, 75%Co-MnHCFe and pure MnHCFe. The as synthesized powders green color intensity increases with the content of cobalt.

Electrodes preparation. Slurries containing the cobalt-manganese hexacyanoferrates active materials, amorphous carbon (Super P Li) and poly(vinylidene) difluoride (PVDF, Kynar HSV900) in a ratio of 80:13:7 were prepared by grinding these materials by hand, and then dispersing them in 1-methyl-2-pyrolidinone (NMP). Electrodes with mass loadings of about 5 mg/cm^2 were prepared by spreading the slurry on a carbon cloth current collector (Fuel Cell Earth/Ballard Avcarb). The electrodes were dried in vacuum at 90°C for two hours.

Electrochemical cell setup. Flooded cells made of a cobalt, manganese hexacyanferrate working electrode, an activated carbon anode, a pH=2, 10 M sodium perchlorate electrolyte and a Ag/AgCl 4M reference electrode were prepared in a nitrogen-filled glove box and tested with a VMP-3 Biologic multichannel potentiostat with an EIS board.

Synchrotron X-ray diffraction. *Ex situ* XRD data was measured at 12 keV at beamline 2-1 at the Stanford Synchrotron Radiation Lightsource. The data was indexed using the CRYSFIRE Powder Indexing System[43], and the lattice parameters/space groups were confirmed with Le Bail fits using GSAS/EXPGUI[44,45]. Rough estimates of crystallite size were generated using the Lorentzian isotropic crystallite size broadening parameter (LX) as outlined in the GSAS manual[44].

In situ XRD data was measured at 15 keV at beamline 7-2 at the Stanford Synchrotron Radiation Lightsource (SSRL). *In situ* diffraction data was collected in transmission mode on a Pilatus 300K image detector and integrated using WxDiff. The data presented in this study was collected at 1-minute intervals with an exposure time of 10 seconds. Rectangular sections of the diffraction image with zero intensity are a result of physical gaps between adjacent detector modules. The electrodes were galvanostatically cycled at a rate of approximately 1C (based on a nominal capacity of 120 mAh g^{-1}) using a Biologic SP-50 galvanostat.

During the *in situ* XRD cycling, the materials change between cubic and rhombohedral phases (**Figure 5 and S6**). For the cubic phase, the lattice parameter was estimated by fitting the position of the d_{200} peak and calculating the lattice parameter. For the hexagonal setting of the rhombohedral phase, which is most distinct in the initial reduced form of MnHCFe, the positions of the d_{202} and d_{220} peaks were fitted and used to calculate the corresponding rhombohedral lattice parameter. Past studies with Rietveld refinement of these materials have shown that ions do not move relative to the lattice even as the phase changes (fractional coordinates remain the same), and both the cubic and rhombohedral lattice parameters correspond to double the distance between adjacent Co/Mn and Fe ions. Thus, changes in the bond length between the cyano ligand and adjacent transition metal ions are directly correlated to changes in the lattice parameter.

Soft X-ray absorption spectroscopy (sXAS). sXAS was performed at Beamline 8.0.1 of the Advanced Light Source (ALS) at Lawrence Berkeley National Laboratory (LBNL). The undulator and spherical grating monochromator supply a linearly polarized photon beam with resolving power up to 6000. The experimental energy resolution is 0.1-0.15 eV. Data were collected in total-electron-yield (TEY) mode with the probe depth of about 10 nm. All the spectra have been normalized to the beam flux measured by the upstream gold mesh. sXAS measurements of the Mn, Fe and Co *L*-edge were conducted on a series of electrodes that were electrochemically cycled to the desired state of charge. All electrodes were vigorously rinsed with acetonitrile and dried in an Ar glove box immediately after cell disassembly to lock the state of charge. Electrodes were transferred into an ultra-high vacuum sXAS end station through our special sample transfer kit to avoid any air exposure. The ultra-high vacuum of sXAS should not affect the samples because they were already dried under vacuum at 90 C before characterization.

sXAS calculations. Atomic multiplet calculations for XAS are based closely on the model and notation previously used in the literature[30]. The configuration averaged energies of different valence states without a core hole is set by parameters $E_{G2} = E_0 - E_L^-$ and $E_{G3} = E_L^- - E_L^+$. The terms E_0, E_L^-, and E_L^+ are respectively the configuration averaged energies with nominal electron number, with a single electron transferred from the metal site to the surrounding cyano groups, or with a single hole transferred from the surrounding cyano groups. Identically defined parameters E_{F2} and E_{F3} apply to the core hole states.

The configuration energies used to describe Fe^{III} at the carbon site are: 10Dq = 4.0 eV, E_{G2} = 0.2 eV, E_{F2} = -0.3 eV, E_{G3} = 1.80 eV, E_{F3} = 2.30 eV. Mixing parameters are 0.9 eV for σ back-bonding, 2.0 eV for π back-bonding, 2.1 eV for σ bonding and 0.6 eV for π bonding.

These parameters are identical to the optimized parameter set for $K_3Fe(CN)_6$[30]. with the exception that E_{L^-} has been raised by 0.8 eV in the ground and intermediate states.

The configuration energies used to describe Fe^{II} at the carbon site are: 10Dq = 3.9 eV, E_{G2} = 3.26 eV, E_{F2} = 2.76 eV, E_{G3} = -3.20 eV, E_{F3} = -1.2 eV. Mixing parameters are 1.2 eV for σ back-bonding, 1.92 eV for π back-bonding, 2.28 eV for σ bonding and 0.0 eV for π bonding. These parameters are identical to the optimized parameter set for $K_4Fe(CN)_6$[30], with the exception that E_{L^-} has been lowered by 1.2 eV in the ground and intermediate states, and all mixing parameters have been increased by 20%.

N-site Fe calculations use reduced 10Dq values to achieve a high spin state and are performed without a back-bonding mixing parameter[28]. The configuration energies used to describe Fe^{III} at the N site are: 10Dq = 1.0 eV, E_{G2} = 1.0 eV, E_{F2} = 0.5 eV, E_{G3} = -1.5 eV, E_{F3} = 1.0 eV. Mixing parameters are 0 eV for back-bonding, 2.1 eV for σ bonding and 0.6 eV for π bonding. The configuration energies used to describe Fe^{II} at the N site are: 10Dq = 0.7 eV, E_{G2} = 2.06 eV, E_{F2} = -4 eV, E_{G3} = -2 eV, E_{F3} = 1.0 eV. Mixing parameters are 0 eV for back-bonding, 1.9 eV for σ bonding and 0 eV for π bonding.

Calculations for N-coordinated atoms (Mn, Co) use reduced 10Dq values to achieve high spin states and are performed without a back-bonding mixing parameter, which is consistent with previous work[28,30]. The configuration energies used to describe 3+ valence atoms at the nitrogen site are: E_{G2}=0 eV, E_{F2}=0 eV, E_{G3}=-0.5 eV, E_{F3}=-0.5 eV. Mixing parameters are 0 eV for back-bonding, 2.1 eV for sigma bonding, and 0.6 eV for pi bonding. The crystal field strength was set to 10Dq=1.0 eV for Mn^{3+} and 10Dq=2.0 eV for Co^{3+}.

The configuration energies used to describe 2+ valence at the nitrogen site are: E_{G2}=-0.06 eV, E_{F2}=-0.44 eV, E_{G3}=2.0 eV, E_{F3}=0 eV. Mixing parameters are 0 eV for back-bonding and pi bonding. The sigma bonding mixing parameter was set to 1.9 eV for Co^{2+} and 1.1 eV for Mn^{2+}. The crystal field strength was set to 10Dq=0.5 eV for Mn^{2+} and 10Dq=0.7 eV for Co^{2+}.

Parameters for the multipole part of the Coulomb interactions were obtained from Hartree-Fock with slater integrals renormalized to 80%. Ground states were Boltzmann-weighted to T=300 K.

Transmission Electron Microscopy (TEM) with Energy Dispersion Spectroscopy (EDS). Morphology and elemental mapping experiments were carried out in a Tecnai G2 F20 X-Twin TEM at the acceleration voltage of 200 kV. To avoid the peak overlaps, a Au grid was used for clear determination of the transition metal ion concentrations. The results, reported in Fig. 1c include a TEM image, Co L, Fe K, Mn K, and Fe L maps performed on a segment of each particle. We chose the Co L peak in CoHCFe due to the overlap of Co K and Fe L peaks. Likewise, Mn L and Fe K peaks overlap in MnHCFe so Fe L map was induced to confirm the homogeneous distribution inside the particles.

X-ray Photoelectron Spectroscopy (XPS). We probed the oxidation states of the electrode materials by taking high resolution X-ray photoelectron spectroscopy (XPS) scans of the Co

2p3, Mn 2p3/2 and Fe 2p3/2 region using PHI-5000 Versaprobe (ULVAC-PHI Inc., Osaka, Japan). Spectra were plotted without further processing.

Thermogravimentric Analysis (TGA). Thermal analysis was performed by a Mettler Toledo - 1 Star System TGA/DSC equipped by a Pfeiffer gas mass analyzer. The temperature was scanned between room temperature and 400°C at 2°C min^{-1} in a helium atmosphere.

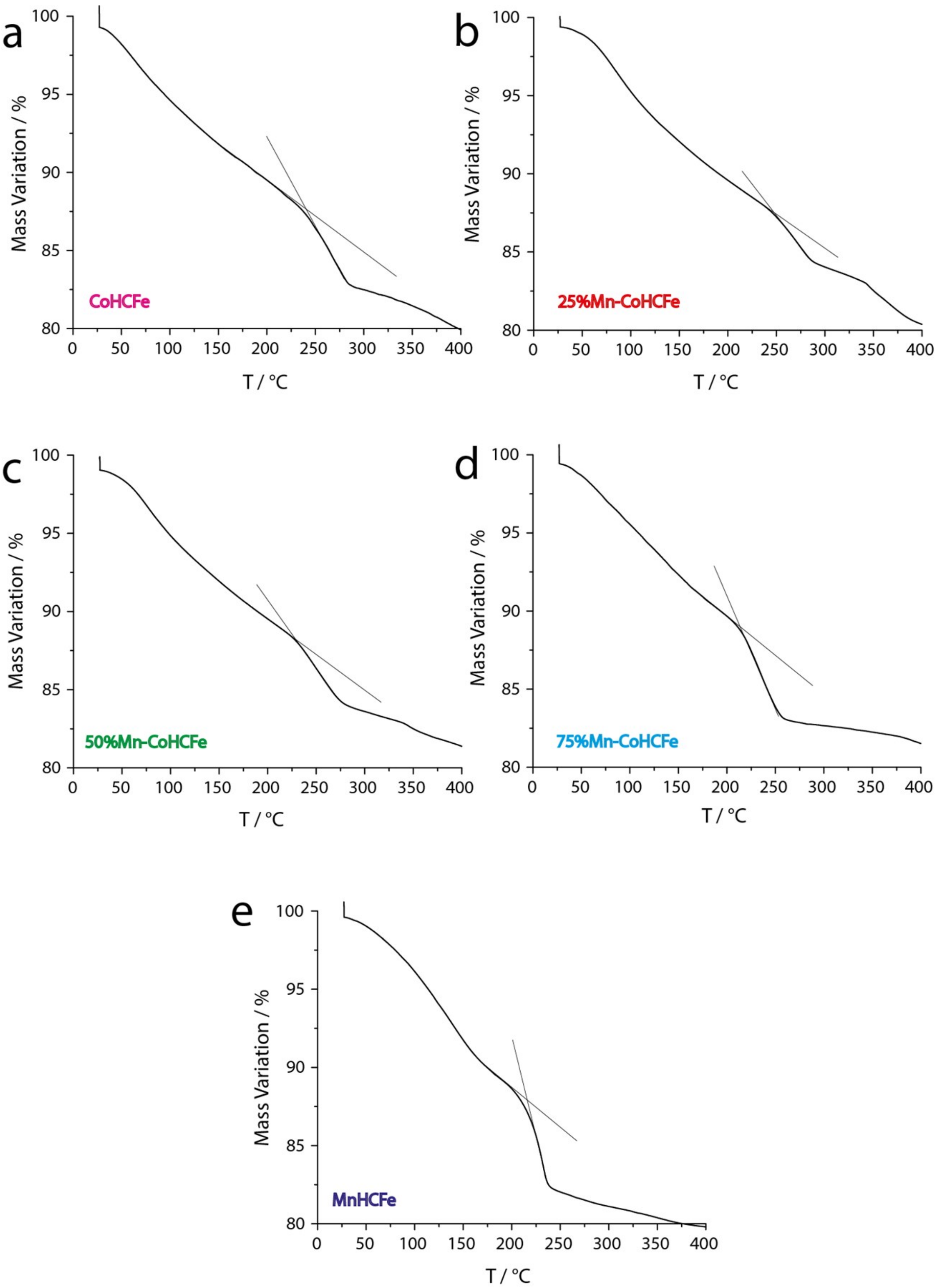

Figure S1. Thermogravimetric analysis of as-synthesized powders. Thermogravimetric analysis (TGA) with differential scanning calorimetry (DSC) of the as synthesized Mn-CoHCFe hybrids. (a) CoCHFe, (b) 25%Mn-CoHCFe, (c) 50%Mn-CoHCFe, (d) 75%Mn-CoHCFe and (e)

MnHCFe. The thin lines indicate where the slope of the curve changes, which corresponds to the decomposition of the material.

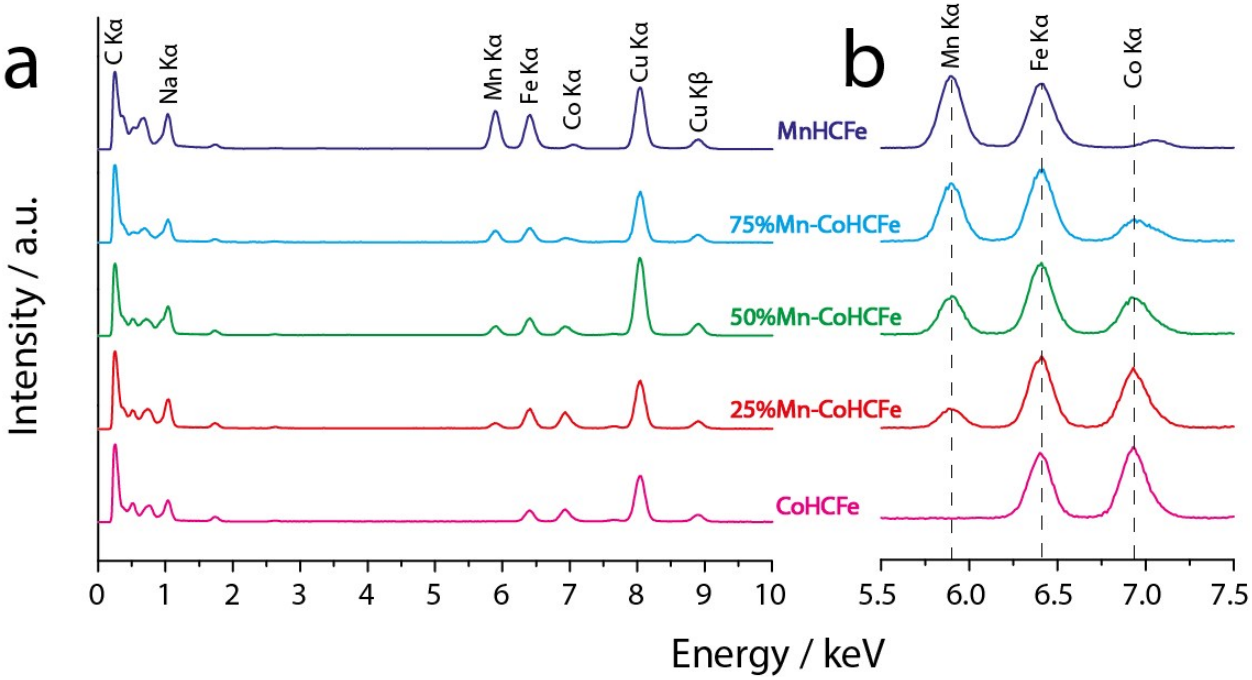

Figure S2. Elemental composition of as-synthesized powders. (a) Energy-dispersive X-ray spectroscopy (EDX) of the as synthesized Mn-CoHCFe hybrids, (b) zoom in in the Mn, Fe, Co kα transitions.

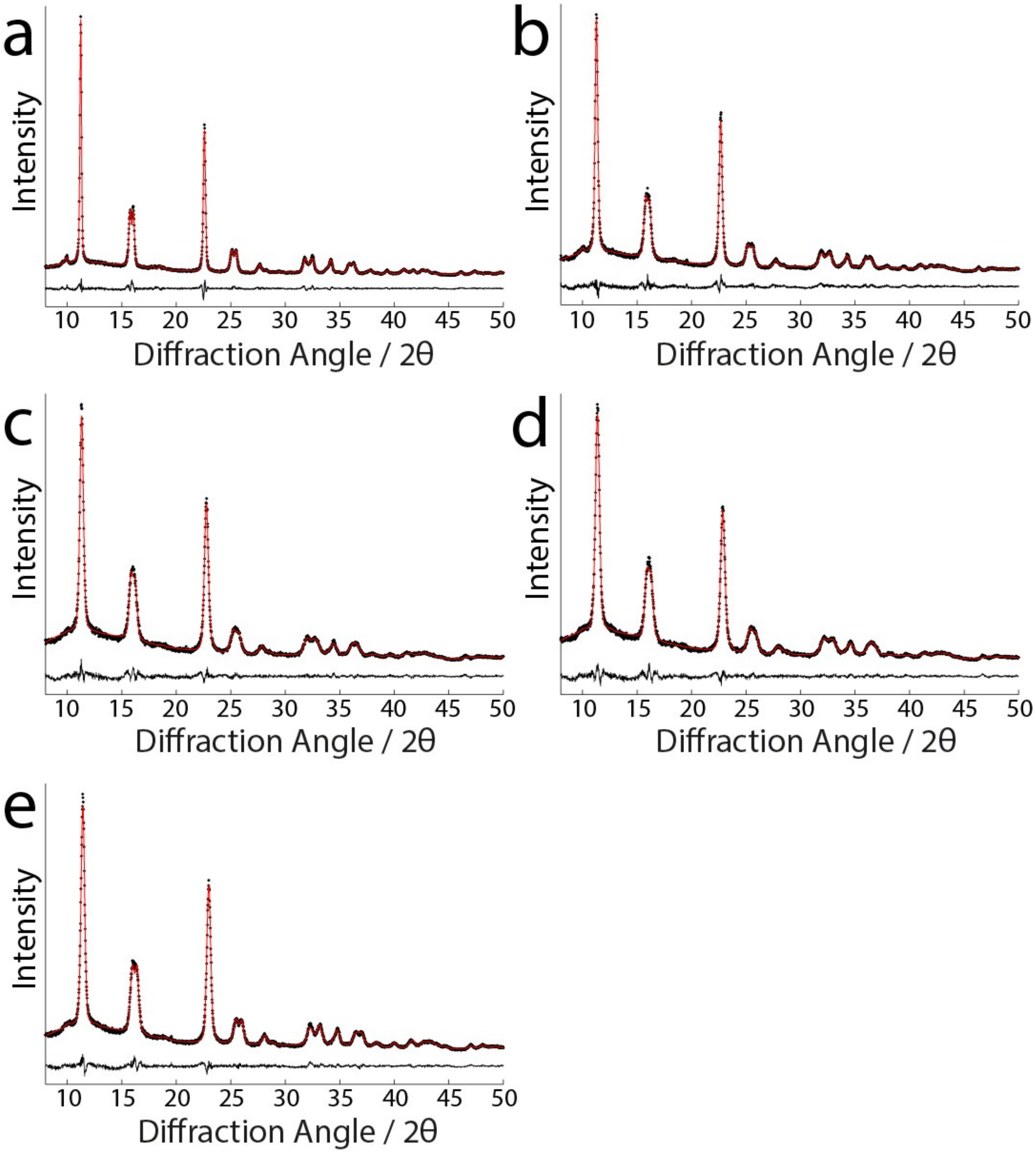

Figure S3. Le Bail fitts of XRD data for as-synthesized powders. The synchrotron XRD data and Le Bail fits for as-synthesized a) MnHCFe, b) Mn/CoHCFe (75% Mn), c) Mn/CoHCFe (50% Mn), d) Mn/CoHCFe (25% Mn), and e) CoHCFe are shown. All of the peaks can be indexed and fit to the R-3m rhombohedral space group (hexagonal setting).

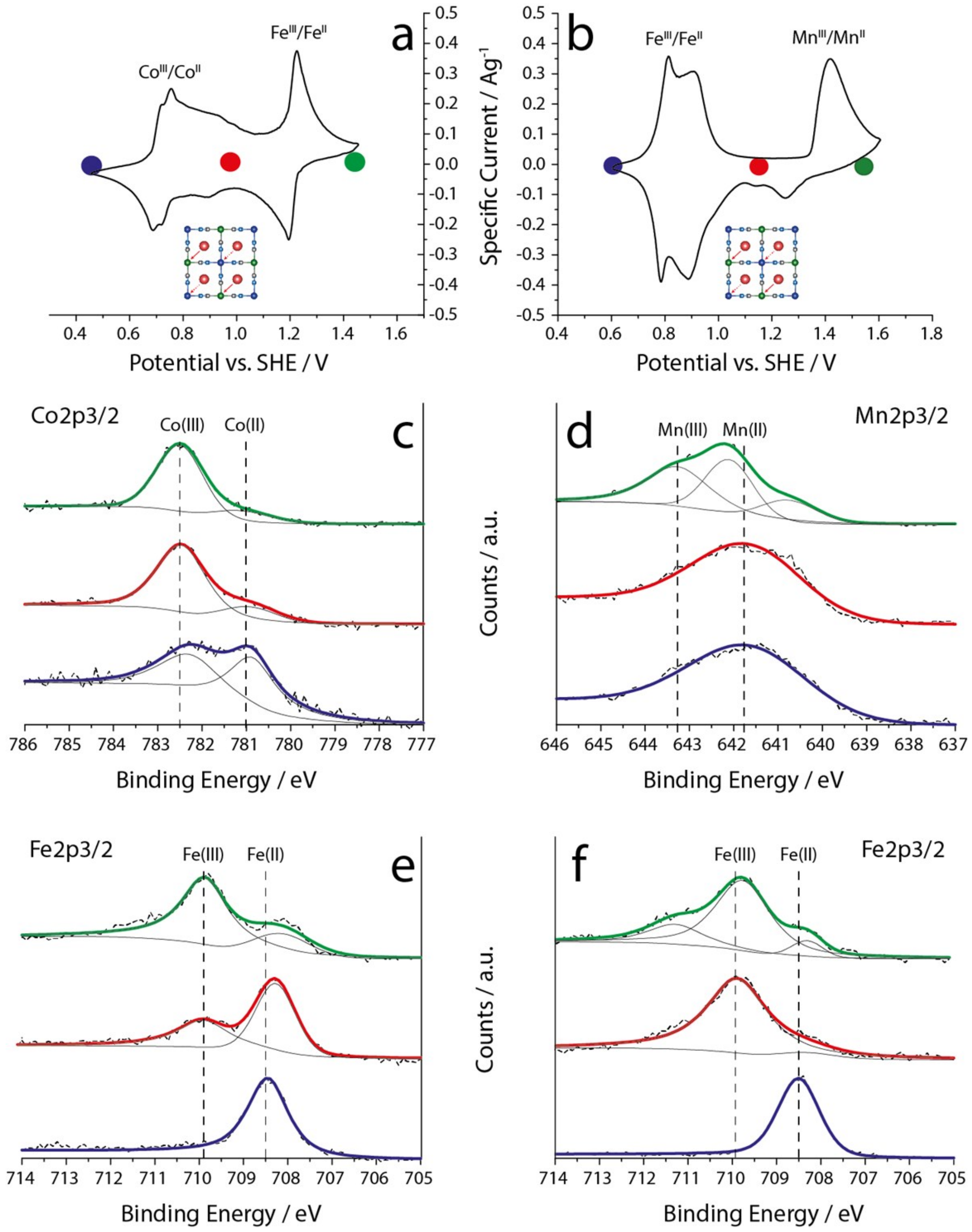

Figure S4. CoHCFe and MnHCFe electrochemistry. The cyclic voltammograms (CV) of (**a**) CoHCFe and (**d**) MnHCFe in a pH=2, saturated $NaClO_4$ aqueous electrolyte show three electrochemical processes at 0.7, 0.75, and 1.2 V and at 0.8, 0.9, and 1.4 V, respectively. MnHCFe and CoHCFe electrodes for the sXAS studies were galvanostatically charged to three different potentials/charge states represented by the blue (0.6 V for MnHCFe and 0.45 V for CoHCFe), red (1.1 V and 0.95 V, respectively), and green (1.5 V and 1.45 V, respectively) dots. The two lower-potential processes are ascribable to the Na-ion insertion in rhombohedral and cubic phases, respectively. X-ray photoelectron spectroscopy (XPS) at the Co2p3/2 (**c**) and Fe2p3/2 (**e**) edges prove that the N-coordinated Co is electrochemically active at lower potentials, while at 1.2 V it is the C-coordinated Fe that changes its valence state. The CV of

MnHCFe (**b**) in the same electrolyte also displays three electrochemical processes. The two lower-potential processes are ascribable to the Na-ion insertion in rhombohedral (0.8 V) and cubic (0.9 V) phases. XPS at the Mn2p3/2 (**d**) and Fe2p3/2 (**f**) edges confirm that both processes are ascribable to the electrochemical activity of the C-coordinated Fe (Mn^{II}—N≡C—$Fe^{III/II}$). The N-coordinated Mn is instead responsible for the poorly reversible electrochemical process at 1.4 V ($Mn^{II/III}$—N≡C—Fe^{III}).

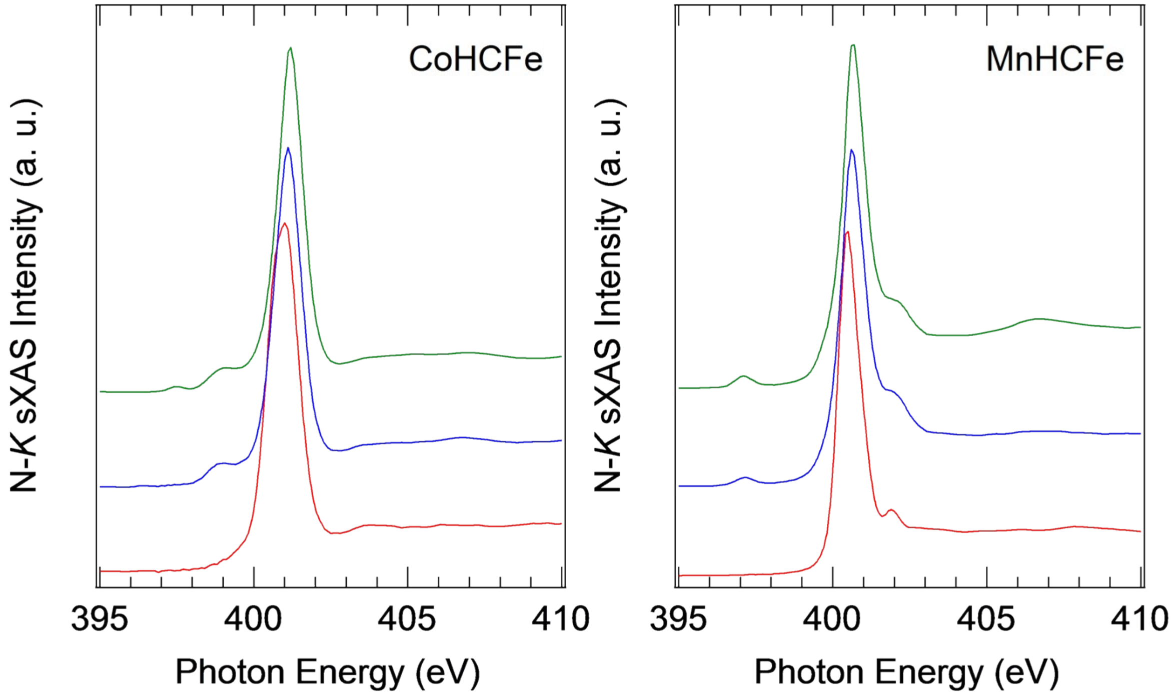

Figure S5. N K-edge sXAS spectra. N K-edge sXAS spectra were collected at a series of CoHCFe and MnHCFe electrode samples that are at different states of charge. In the N K-edge sXAS spectra, the main absorption peaks around 401eV originated from the CN π* orbital. The energy shifts of the main peaks in the N-K spectra indicate the chemical potential change during the electrochemical operation, i.e., high oxidation states in the charged electrodes lead to higher energy values of the main peak, compared with the pristine electrodes.

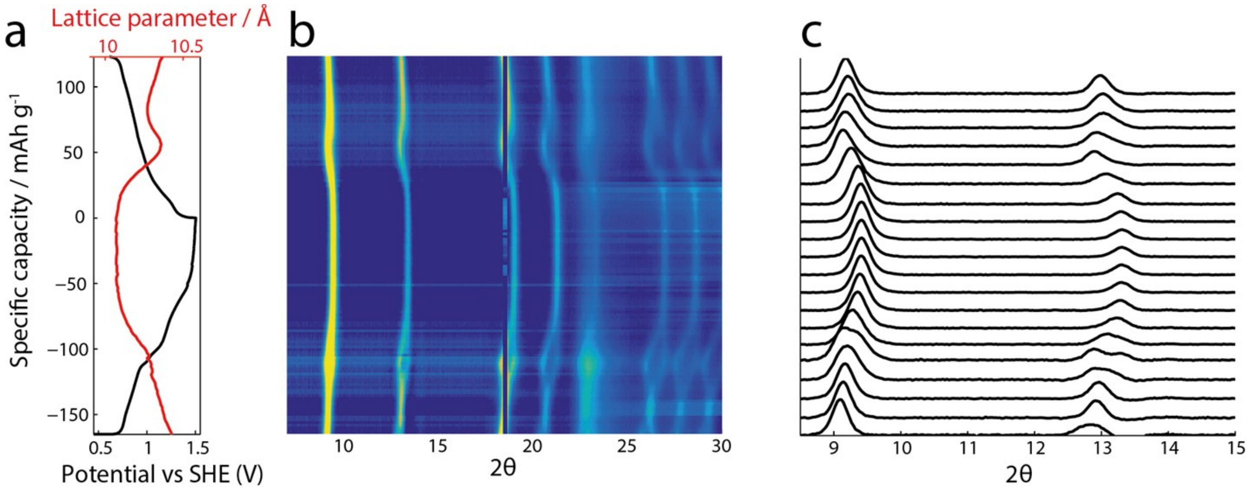

Figure S6. In situ XRD of the 50% Mn-CoHCFe. The 50% Mn-CoHCFe shows features that are similar to those of both pure CoHCFe and MnHCFe. During charging, a clear plateau is observed around 0.7 V, which is a result of the complex combination of the electrochemical activity of the N-coordinated Mn and Co (**Figure S3c**). Previous studies on lithium insertion in mixed Mn/CoHCFe suggest that Mn and Co are concurrently oxidized at the lower plateau[34]. As the potential increases, we can observe a brief phase separation, which is a result of anisotropic Jahn-Teller distortion upon formation of Mn(III). The two phases merge back into a single phase upon further oxidation and contraction of the lattice. The contracted lattice suppresses the redox voltage of Mn(II/III) and stabilizes low-spin Mn(III), which alleviates the Jahn-Teller distortion[34]. The upper plateau corresponds to the oxidation of the C-coordinated Fe, which does not have a major impact on either lattice parameter or crystal structure. It is interesting to note that Mn becomes electrochemically active at a lower potential in the hybrid MnCoHCFe than in the pure MnHCFe. This may be due to interactions in the spin coupling of Mn, Co, and Fe in this mixed phase. The lattice contraction (driven by formation of Co(III)) stabilizes the low-spin Mn(III) state and suppresses the redox voltage[34,40]. In situ magnetic measurements will be required to further explore this behavior[41]. During the discharge step, the processes just described are reversed. The bump in the equivalent lattice parameter observed at 220 mAh g^{-1} may result from the combination of the electrochemical activity of N-coordinated Mn (a brief return of the Jahn-Teller distortion of Mn(III)) in addition to evolving spin states and hybridization in the Mn, Co, and Fe atoms. Upon further oxidation, the structure stabilizes and returns to its original form.

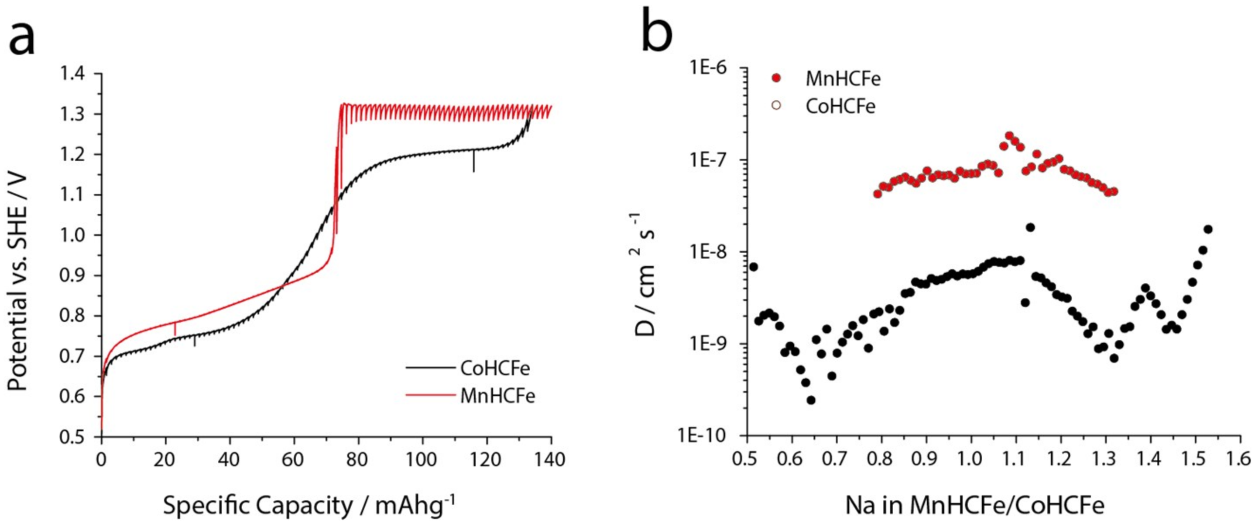

Figure S7. GITT. (a) Potential vs. specific capacity profile and (b) diffusion coefficient as a function of the state of charge.

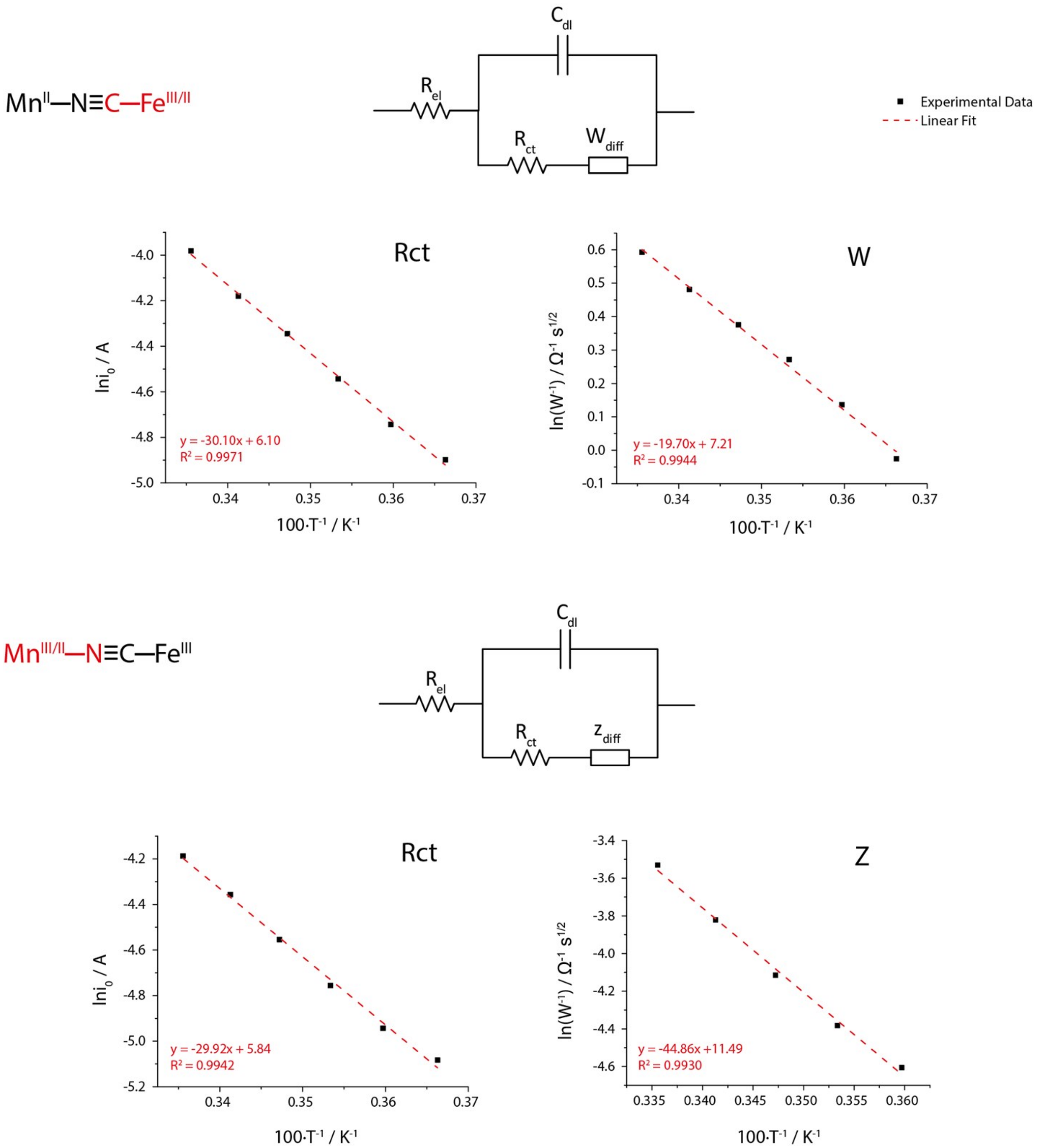

Figure S8. Arrhenius plots for MnHCFe. Arrhenius plots of the different elements in the equivalent circuit show the temperature dependence of these processes.

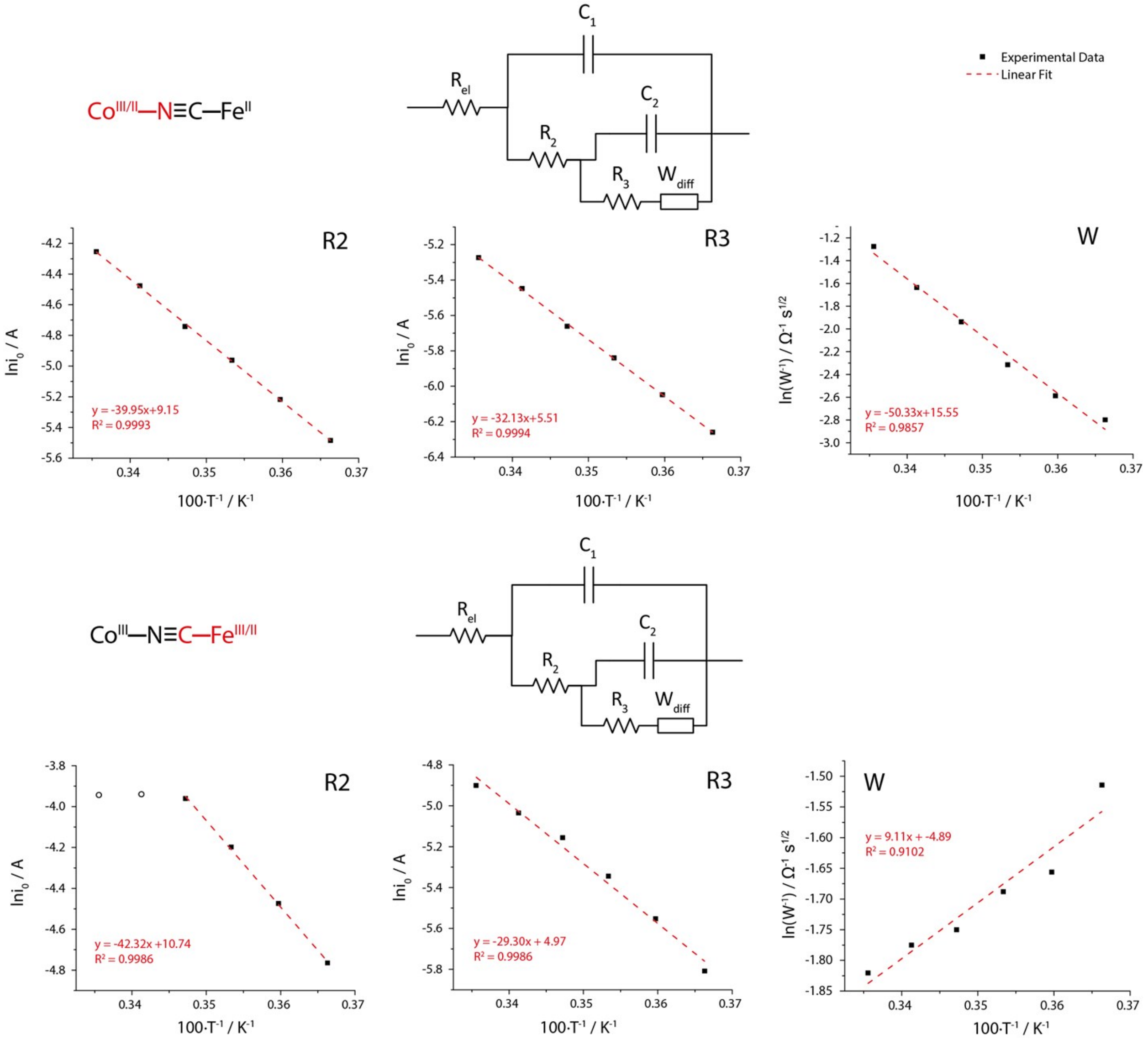

Figure S9. Arrhenius plot for CoHCFe. Arrhenius plots of the different elements in the equivalent circuit show the temperature dependence of these processes. The deviation from linearity for the processes associated with Fe may be due to the extensive orbital hybridization within CoHCFe. The distinction between processes is not as neat as in the case of MnHCFe, and the contribution of both ions is observed.

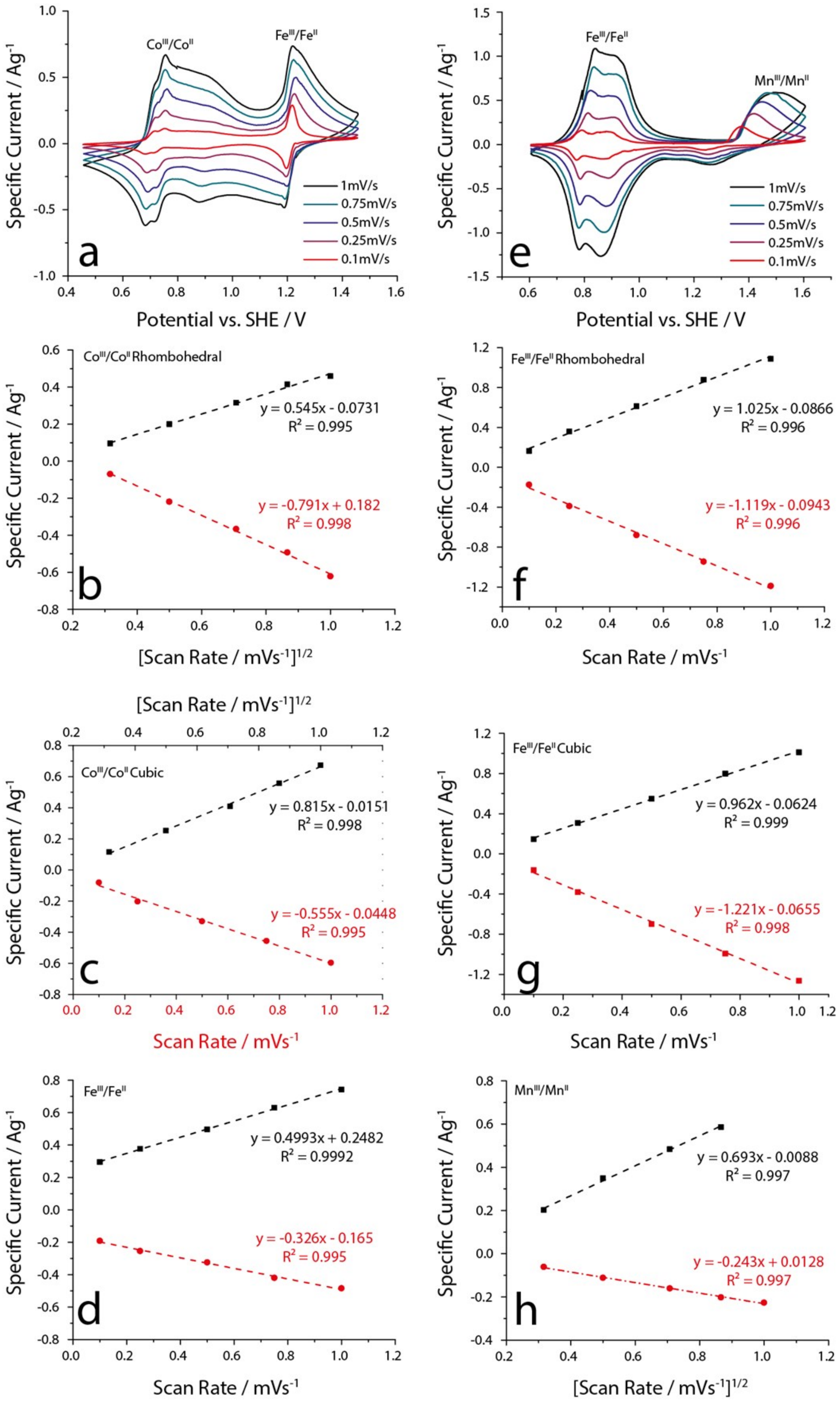

Figure S10. Cyclic Voltammetry investigation. CVs of (**a**) MnHCFe and (**e**) CoHCFe at different scan rates (0.1, 0.25, 0.5, 0.75, 1 mV s^{-1}). Peak current intensities versus scan rate plots of the cubic and rhombohedral peaks of MnHCFe (**f**,**g**) and of the C-coordinated (Co^{III}—N≡C—Fe$^{III/II}$) (**d**) show a linear relationship with the scan rate typical of a charge-transfer-limited kinetic regime. The N-coordinated Mn (**h**) process at 1.3 V shows the square-root dependence typical of a diffusion-limited electrochemical process. Similar plots for CoHCFe show how the rhombohedral (**b**) and cubic (**c**) processes associated with the electrochemical activity of the N-coordinated Co ($\mathrm{Co^{III/II}}$—N≡C—$\mathrm{Fe^{II}}$) show the square-root dependence typical of a diffusion-limited electrochemical process.

In the case of MnHCFe, the peaks corresponding to the electrochemical processes at 0.8 and 0.9 V (rhombohedral and cubic, respectively) are both chemically and electrochemically reversible[42]. Moreover, the difference (ΔE_p) between the anodic ($E_{p,a}$) and the cathodic ($E_{p,c}$) peak potentials is less than the 57 mV predicted for a monoelectronic, diffusion-limited process at 25 °C[42]. This is a clear indication of a *diffusionless behavior*, wherein the maximum current is limited by the charge-transfer step and consequently by the number of electroactive species at/in the electrode. This behavior is typical of thin film electrodes[43,44], and, to the best of our knowledge, it was previously reported in bulk systems only for PBAs in aqueous electrolyte[45]. In the thin film electrode treatment, a linear relationship between the peak current and the scan rate is observed according to the following equation[43]:

$$i_{peak} = \frac{n^2 F^2}{4RT} \times A \times \Gamma_0^* \times \upsilon \qquad (1)$$

where *n* is the number of electrons involved in the reaction, *F* the Faraday constant (C $\mathrm{mol^{-1}}$), *R* the gas constant (J $\mathrm{mol^{-1}\ K^{-1}}$), *T* the temperature (K), *A* the surface area ($\mathrm{cm^2}$), Γ_0^* the concentration of active sites (mol $\mathrm{cm^{-2}}$), and *v* the scan rate (mV $\mathrm{s^{-1}}$). Both cathodic and anodic peaks in **Figure S10f-g** show the predicted linear relationship with the scan rate, thus confirming the charge-transfer-limited kinetic regime. The Γ_0^* parameters obtained from the slopes of the linear fits can be used to calculate the specific capacity of each electrochemical process; the specific charge involved in the oxidation and reduction of rhombohedral and cubic $\mathrm{Fe^{III/II}}$ are estimated as 30±2 and 31±4 mAh $\mathrm{g^{-1}}$, respectively. Both cubic and rhombohedral peaks show the same kinetic behavior because they are associated with the same electrochemical process: $\mathrm{Mn^{II}}$—N≡C—$\mathrm{Fe^{III/II}}$.

On the contrary, the N-coordinated Mn ($\mathrm{Mn^{III/II}}$—N≡C—$\mathrm{Fe^{III}}$) process at 1.3 V is both chemically ($i_{p,c} \ll i_{p,a}$) and electrochemically ($\Delta E_p \gg 59$ mV) irreversible. We believe that the chemical irreversibility is caused by two factors: the competing oxidation reaction of the aqueous electrolyte at high voltage and irreversibly evolving electronic states and hybridization across the cyano groups, which we discuss in detail in the crystallography section above. The electrochemical irreversibility is instead the result of the phase separation triggered by the Jahn-Teller distortion associated with the formation of $\mathrm{Mn^{III}}$ [39]. This behavior can be modeled with a *diffusion-controlled* kinetic regime in which the peak current depends linearly on the square root of the scan rate (**Figure S10h**), whose dependency is given by[43]:

$$i_{peak} = 0.4463 \times \sqrt{\frac{n^3 F^3}{RT}} \times A \times \sqrt{D} \times C_0 \times \sqrt{\upsilon} \qquad (2)$$

where *D* is the average diffusion coefficient ($\mathrm{cm^2\ s^{-1}}$) in the whole composition range and C_0 the concentration of active sites (mol $\mathrm{cm^{-3}}$). The slope can usually be used to determine the diffusion coefficient once C_0 and *n* are known. In this specific case, the chemical irreversibility associated with the process make this calculation less meaningful.

Table 1. Peak Positions at 0.5mV/s.

	$\mathrm{Mn^{II}}$—N≡C—$\mathbf{Fe^{III/II}}$	$\mathbf{Mn^{III/II}}$—	$\mathbf{Co^{III/II}}$—N≡C—$\mathrm{Fe^{II}}$	$\mathrm{Co^{III}}$—N≡C—$\mathbf{Fe^{III/II}}$

	Rhombohedral	**Cubic**	N≡C—Fe^{III}	**Rhombohedral**	**Cubic**	
Anodic Peak Potential /mV	0.822	0.899	1.447	0.730	0.762	1.229
Cathodic Peak Potential /mV	0.784	0.878	1.252	0.689	0.721	1.197
ΔE_p / mV	39.08	20.6	194.5	40.9	40.9	32.3

In the case of CoHCFe, the interpretation of the results is more challenging. The rhombohedral and cubic processes in the 0.7 V region associated with the electrochemical activity of the N-coordinated Co (Co$^{III/II}$—N≡C—Fe^{II}) are both chemically and electrochemically reversible. Moreover, they both show a ΔE_p below 59 mV (40.9 mV) that is usually a symptom of a charge-transfer-limited kinetic regime (**Table 2**). Nonetheless, the relationship between scan rate and peak current shows the square-root dependence typical of a diffusion-limited electrochemical process (**Figure S10b-d**). We believe that these phenomena may reflect the spin-state transition and changing hybridization associated with this reaction. Only the cathodic scan of the cubic process (**Figure S10b**, red line) can be fitted with **Equation 2**. If we consider the reaction as monoelectronic and estimate C_0 from the specific capacity (25 mAh g^{-1}), we can calculate the diffusion coefficient D of Na$^+$ to be $2.1\pm1.0\text{x}10^{-9}$ cm^2 s^{-1}. This value is in good agreement with the GITT diffusion coefficients reported in **Figure S5b**.

The process at 1.2V, corresponding to the electrochemical activity of the C-coordinated Fe (Co^{III}—N≡C—Fe$^{III/II}$), is both chemically and electrochemically reversible and can be well fitted with **Equation 2**, thus supporting the charge-transfer-limited process observed in the CV study.